



# Physics-informed neural networks for studying heat transfer in porous media



Jiaxuan Xu <sup>a,b</sup>, Han Wei <sup>a,b</sup>, Hua Bao <sup>a,b,\*</sup>

<sup>a</sup> Global Institute of Future Technology, Shanghai Jiao Tong University, Shanghai 200240, China

<sup>b</sup> University of Michigan-Shanghai Jiao Tong University Joint Institute, Shanghai Jiao Tong University, Shanghai 200240, China

## ARTICLE INFO

### Keywords:

Porous media  
Physics-informed neural network  
Effective thermal conductivity  
Temperature and heat flux fields

## ABSTRACT

Numerous efforts have been devoted to studying heat transfer problems in porous media. Physics-based models, numerical methods and experiments are commonly adopted to obtain the temperature and heat flux fields, along with effective thermophysical properties like effective thermal conductivity for heat conduction, which exert significant impact on analyzing the heat transfer efficiency in porous systems. Recently, using data-driven machine learning methods to predict temperature/heat flux fields and effective thermal conductivity of porous media has gained attention, demonstrating the potential to achieve higher accuracy than physics-based models while requiring less computational time than numerical methods. However, machine learning approaches are commonly restricted by the requirement for sufficient labeled training data, which can be difficult and time-consuming to acquire. In this work, we apply physics-informed neural networks to investigate heat conduction in porous media. We show that, without any labeled training data, accurate predictions for temperature/heat flux fields in porous media can be achieved. The obtained effective thermal conductivity values for an ensemble of porous media samples have an average relative error of only 2.49%. Compared with numerical calculations, a computation acceleration of 5 orders of magnitude has been achieved. Compared with data-driven machine learning methods, this method offers enhanced flexibility since no labeled data is required. Furthermore, we also illustrate that physics-informed neural networks can be easily extended to predict nonlinear heat conduction in porous media. Our work demonstrates that physics-informed neural networks are promising tools for studying heat conduction problems and can also be possibly extended to study other complex heat transfer problems in porous media.

## 1. Introduction

Porous media widely exist in engineering applications, such as thermal barrier coatings in aeroengine blades for thermal insulation [1], open-cell metallic foams in compact heat exchangers for increased internal surfaces [2], porous silicon nanowires as thermoelectric materials for enhanced figure of merit [3], and porous thermal metamaterials for controlling heat and mass transfer [4–6]. Heat transfer in these porous media can exert a significant impact on energy conversion and thermal management in practical applications [7,8]. The overall efficiency of heat transfer is significantly influenced by heat conduction within porous media, which is commonly evaluated by two critical thermophysical characteristics: the effective thermal conductivity of porous media, as well as the temperature and heat flux fields during heat conduction [9–12]. Efficiently predicting the effective thermal conductivity

and temperature/heat flux fields of porous media can accelerate the design of porous systems to improve energy efficiency [13].

Numerous investigations have explored heat conduction in various porous media [8,14–16], including cellular [2], fibrous [17], and granular porous media [18]. To predict the effective thermal conductivity of porous media, the effective medium theory (EMT) is widely applied to develop simple analytical models that provide fast predictions but limited accuracy [19–22]. On the other hand, accurate effective thermal conductivity and temperature/heat flux fields can be obtained from numerical calculations that directly solve heat conduction equations [15,23–28]. However, numerical calculations are commonly used for case-by-case calculations and require a high computational cost [26,27]. Recently, advances in data-driven machine learning methods have inspired growing interest across diverse disciplines, owing to the ability to develop accurate and fast surrogate models based on data analysis [29–34]. In particular, data-driven machine learning methods have

\* Corresponding author.

E-mail address: [hua.bao@sjtu.edu.cn](mailto:hua.bao@sjtu.edu.cn) (H. Bao).

Nomenclature	
<i>Latin Symbols</i>	
x	Spatial coordinates, a.u.
T	Local temperature, a.u.
T	Temperature field, a.u.
q	Local heat flux vector, a.u.
Q	Heat flux field, a.u.
n	The unit normal vector for the Neumann boundary
V <sub>p</sub>	Porosity, %
n	Total number of uniform grids in a porous media image
M	Total number porous media in the test dataset
y	Output channels of the neural network, a.u.
<i>Greek Symbols</i>	
$\kappa$	Thermal conductivity, a.u.
$\kappa$	Thermal conductivity distribution, a.u.
$\Gamma$	Physical domain, a.u.
<i>Subscripts</i>	
D	Dirichlet boundary
N	Neumann boundary
i	The index of output channels of the neural network
j	The index of porous media in the test dataset
k	The index of grid in the porous media image

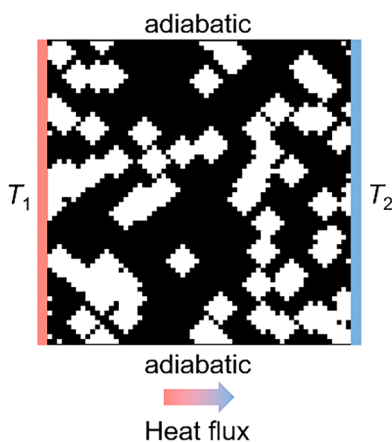


**Fig. 1.** Illustration of heat conduction in a porous media. The white and black regions represent the pore and matrix phases, respectively. The left and right boundaries are Dirichlet boundaries with temperatures  $T_1$  and  $T_2$ . The top and bottom boundaries are both adiabatic.

proven effective in studying heat conduction in porous media [13, 35–38]. For example, Wei et al. [35] employed a convolutional neural network (CNN) to predict the effective thermal conductivity of porous media, achieving high accuracy and negligible time required for predicting. By constructing a convolutional encoder-decoder neural network, Wang et al. [38] also demonstrated that the temperature field in porous media can be accurately predicted through data-driven analysis. As an image-to-image regression model widely used for image denoising and reconstruction [39], this method yields speedups of several orders of magnitude compared to numerical calculations when predicting the temperature field of the input porous media images. However, a major deficiency of data-driven machine learning methods is that sufficient labeled data is required to constrain the training process and achieve high prediction accuracy [38,40,41]. Although the labeled training data can theoretically be obtained using any method with good

accuracy, in practice, they are commonly obtained from numerical calculations that require solving physics-based partial differential equations. Acquiring substantial amounts of labeled training data is usually challenging, which hinders the application of data-driven machine learning methods for efficient prediction of heat conduction in different porous media [42–44].

One potential strategy for mitigating the reliance on the labeled data, while also leveraging the high accuracy and computational speed of machine learning models, is to incorporate the known governing physical equations to constrain the training process. Built upon this idea, physics-informed neural networks (PINNs) have emerged to solve forward and inverse physical problems by constructing loss functions based on the residual of governing partial differential equations (PDEs) instead of labeled data [42,45,46]. By minimizing deviations from the physical laws in the outputs during training, PINNs can learn solutions to PDEs in high-dimensional parameterized spaces (e.g., geometry, equation parameters, initial/boundary conditions), avoiding case-by-case calculations as traditional numerical methods [47–53]. Previous studies have shown that PINNs are capable of efficiently solving various physical problems in regular domains [30] and irregular domains [54] with limited or even zero labeled training data [55,56]. Therefore, this labeled-data-free feature gives PINNs significant potential in efficiently predicting heat transfer in various porous media, but it remains understudied.

In this work, we employ labeled-data-free PINNs to predict heat conduction in various porous media. A convolutional encoder-decoder neural network with physics-informed loss functions is built and trained to minimize the residuals of the governing equations and boundary conditions in the absence of labeled training data. To ensure the generalization capability of the neural network, we generate porous structures with a wide range of porosity and various morphologies as inputs for both training and testing. The trained neural network is subsequently applied to predict the effective thermal conductivity and temperature/heat flux fields during heat conduction for porous structures in the test datasets. The prediction accuracy and time cost of the PINNs are examined by comparing them with data-driven neural networks and numerical calculations. Moreover, using nonlinear heat conduction in porous media under large temperature gradients as an example, we also investigate the effectiveness and flexibility of extending the present method to solve more complex physical problems in porous media.

## 2. Physical problem

We focus on heat conduction in the porous media with granular pores as illustrated in Fig. 1. The governing equations are given by [57]:

$$-\kappa(T, \mathbf{x}) \nabla T(\mathbf{x}) = \mathbf{q}(\mathbf{x}), \mathbf{x} \in \Gamma, \quad (1)$$

$$\nabla \cdot [\kappa(T, \mathbf{x}) \nabla T(\mathbf{x})] = 0, \mathbf{x} \in \Gamma. \quad (2)$$

Here,  $T$  and  $\mathbf{q}$  represent the temperature and the heat flux vector at the spatial coordinate  $\mathbf{x}$  in domain  $\Gamma=[0, 1] \times [0, 1]$ . The unit of the domain size is arbitrary. The thermal conductivity  $\kappa$  ( $\kappa_1$  for matrix phase and  $\kappa_2$  for pore phase) is determined by both the spatial coordinate  $\mathbf{x}$  and the temperature. For linear heat conduction in porous media,  $\kappa_1$  and  $\kappa_2$  are constants and remain independent of temperature. In the case of nonlinear heat conduction,  $\kappa_1$  and  $\kappa_2$  vary with temperature. Moreover, the boundary conditions are given by [57]:

$$\begin{aligned} T(\mathbf{x}) &= T_1, \mathbf{x} \in \Gamma_{D1}, \\ T(\mathbf{x}) &= T_2, \mathbf{x} \in \Gamma_{D2}, \\ \mathbf{q}(\mathbf{x}) \cdot \mathbf{n} &= 0, \mathbf{x} \in \Gamma_N, \end{aligned} \quad (3)$$

where  $\Gamma_{D1}$  and  $\Gamma_{D2}$  are Dirichlet boundaries with dimensionless temperature  $T_1=1$  and  $T_2=0$ , as shown by the left and right boundaries in Fig. 1.  $\mathbf{n}$  is the unit normal vector for the Neumann boundary  $\Gamma_N$  that is

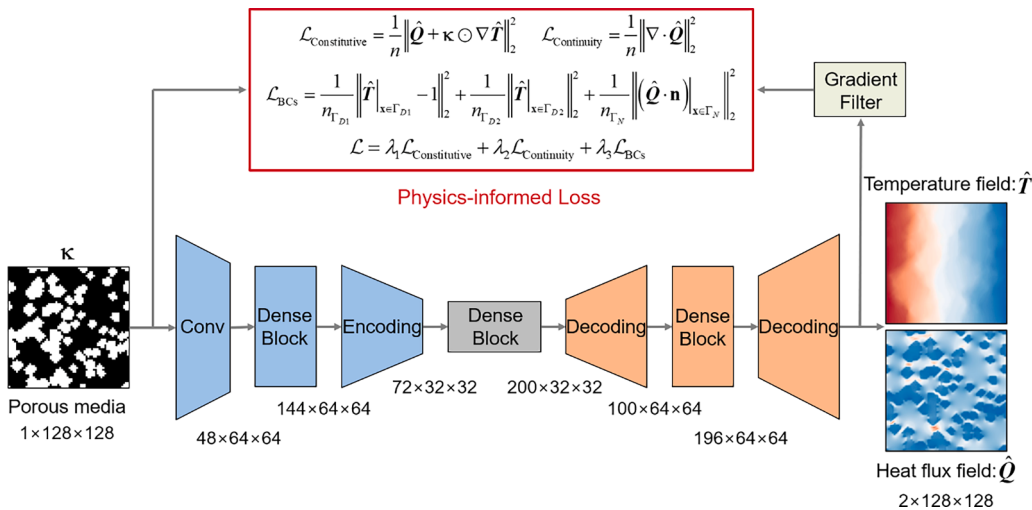


**Fig. 2.** Physics-informed convolutional encoder-decoder neural network maps the input porous media to desired thermophysical characteristics (e.g., the temperature and heat flux fields during heat conduction). The neural network comprises two components, i.e., the encoder network and the decoder network. Physics-informed loss functions can be constructed, which constrain the training of the neural network using the physical governing equations without labeled data.

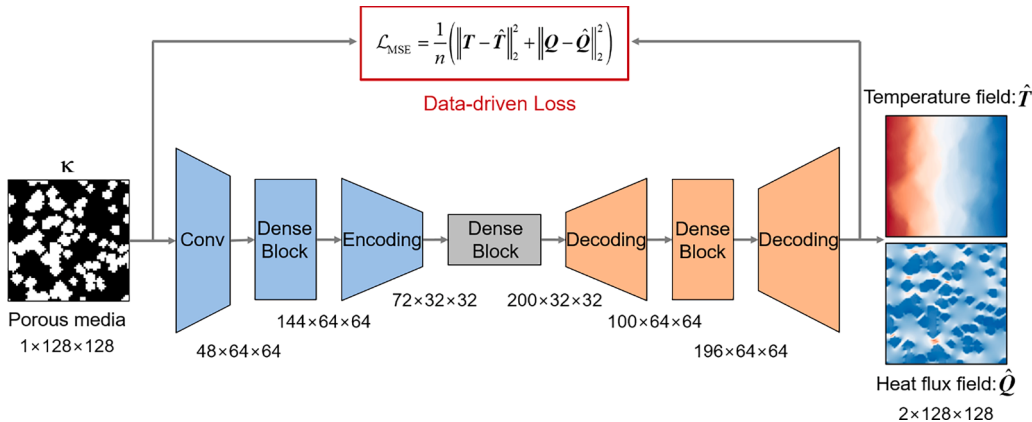


**Fig. 3.** Data-driven convolutional encoder-decoder neural network with the same architecture as the physics-informed convolutional encoder-decoder neural network shown in Fig. 2, utilizing labeled data to formulate data-driven loss functions and constrain the training of the neural networks.

adiabatic as shown by the top and bottom boundaries in Fig. 1. Under these boundary conditions, a temperature gradient is formed from the left to the right of the porous media, where the heat flux is along the  $x$  direction. We aim to develop surrogate models that enable fast prediction of temperature/heat flux fields and the effective thermal conductivity for any input porous media with different porosity and morphologies, using deep learning neural networks.

### 3. Methodology

In this section, we develop a PINN that can be applied for mapping the porous media to the desired thermophysical characteristics by using the known physical governing equations and boundary conditions to constrain the training process. Taking heat conduction in porous media as a simple example (as shown in Section 2), both the principles of the built neural networks and applied datasets of porous media are introduced.

#### 3.1. Physics-informed neural networks

The neural network is a widely applied machine learning method for mapping inputs to outputs in regression problems [58]. In this work, we aim to predict temperature/heat flux fields in a given porous media

image, which is an image-to-image regression problem. As a widely used image-to-image translation approach, the convolutional encoder-decoder neural network has been proven to be effective in modeling high-dimensional input-output mappings in parametric space [59–61]. This characteristic renders it well-suited for predicting temperature/heat flux fields in the input porous media. Therefore, we build a physics-informed convolutional encoder-decoder neural network as shown in Fig. 2 [40,62]. The input channel is the thermal conductivity distribution  $\kappa$  of the porous media, while the output channels are the temperature field  $\hat{T}$  and the heat flux field  $\hat{Q}$ . In the absence of labeled data (i.e., the accurate temperature field  $T$  and the heat flux field  $Q$  that can be obtained from numerical calculations), a physics-informed loss function can be constructed as shown in Fig. 2. Since the output temperature field  $\hat{T}$  and heat flux field  $\hat{Q}$  need to satisfy governing physical laws Eqs. (1–3), the physics-informed loss  $\mathcal{L}$  takes the form of the residual of governing equations and boundary conditions:

$$\mathcal{L} = \lambda_1 \mathcal{L}_{\text{Constitutive}} + \lambda_2 \mathcal{L}_{\text{Continuity}} + \lambda_3 \mathcal{L}_{\text{BCs}}, \quad (4)$$

$$\mathcal{L}_{\text{Constitutive}} = \frac{1}{n} \|\hat{Q} + \kappa \odot \nabla \hat{T}\|_2^2, \quad (5)$$

$$\mathcal{L}_{\text{Continuity}} = \frac{1}{n} \|\nabla \cdot \hat{Q}\|_2^2, \quad (6)$$

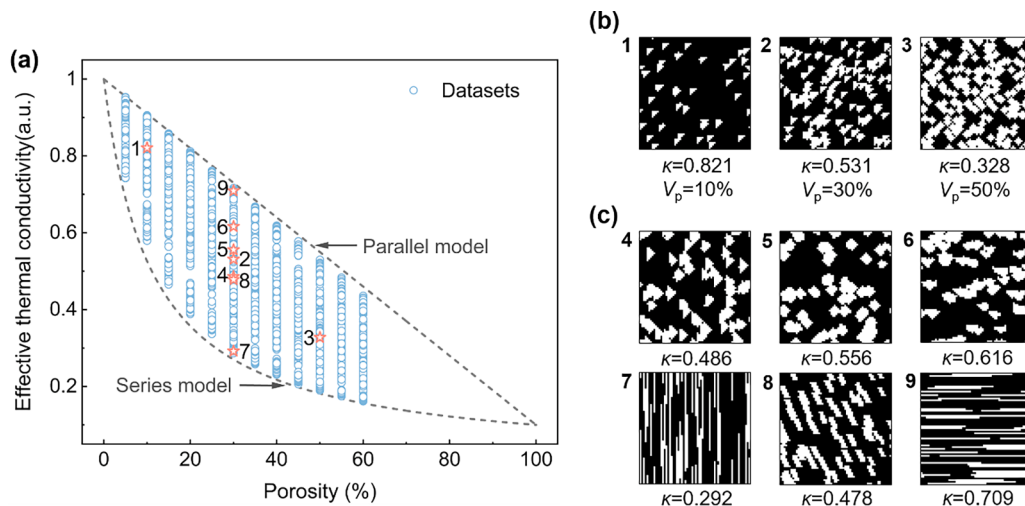


**Fig. 4.** (a) The effective thermal conductivity of 20,254 porous structures with different porosities (symbols), spanning from the upper to the lower limits given by the parallel model and the series model (dashed lines), respectively. The red marks are several representative porous structures. (b) Porous structures 1 to 3 exhibit a decrease in thermal conductivity with increased porosity (from 10% to 50%). (c) Porous structures 4 to 9 exhibit the same porosity of  $V_p = 30\%$  and various porous structures, including highly anisotropic structures (7 and 9), which have diverse thermal conductivity values.

$$\mathcal{L}_{BCs} = \frac{1}{n_{\Gamma_{D1}}} \left\| \widehat{\mathbf{T}}|_{x \in \Gamma_{D1}} - \mathbf{1} \right\|_2^2 + \frac{1}{n_{\Gamma_{D2}}} \left\| \widehat{\mathbf{T}}|_{x \in \Gamma_{D2}} \right\|_2^2 + \frac{1}{n_{\Gamma_N}} \left\| (\widehat{\mathbf{Q}} \cdot \mathbf{n})|_{x \in \Gamma_N} \right\|_2^2. \quad (7)$$

Physics-informed loss terms shown in Eqs. (5-7) are formulated according to the constitutive equation (Eq. (1)), the continuity equation (Eq. (2)), and boundary conditions (Eq. (3)), respectively. Here,  $\lambda_1$ ,  $\lambda_2$  and  $\lambda_3$  are weight coefficients for the three physics-informed loss terms;  $n$  is the total number of uniform grids;  $n_{\Gamma_{D1}}$ ,  $n_{\Gamma_{D2}}$ ,  $n_{\Gamma_N}$  are the grid numbers for the left and right Dirichlet boundaries and the Neumann boundary, respectively. During the training of the PINNs, the total physics-informed loss  $\mathcal{L}$  is minimized to zero, indicating that the output temperature field  $\widehat{\mathbf{T}}$  and heat flux field  $\widehat{\mathbf{Q}}$  are trained to satisfy governing physical laws. Therefore, the known physical knowledge is incorporated via the physics-informed loss, which constrains the training process and eliminates the reliance on labeled data (i.e., the accurate temperature field  $\mathbf{T}$  and the heat flux field  $\mathbf{Q}$  are not required when constructing the loss functions).

### 3.2. Data-driven neural networks

To compare the PINN with data-driven machine learning methods, we also construct a data-driven neural network with the same architecture as the physics-informed convolutional encoder-decoder neural network, but with a different loss function, as shown in Fig. 3. The data-driven loss function is defined as the mean square error (MSE) between the output results and the labeled data:

$$\mathcal{L}_{MSE} = \frac{1}{n} (\| \mathbf{T} - \widehat{\mathbf{T}} \|_2^2 + \| \mathbf{Q} - \widehat{\mathbf{Q}} \|_2^2). \quad (8)$$

The data-driven loss  $\mathcal{L}_{MSE}$  is minimized during the training process, forcing the output temperature field  $\widehat{\mathbf{T}}$  and heat flux field  $\widehat{\mathbf{Q}}$  to approach the accurate temperature field  $\mathbf{T}$  and the heat flux field  $\mathbf{Q}$ . Consequently, the training of data-driven neural networks is constrained by the labeled data. Since neural networks typically require a substantial amount of input data for training, generating extensive labeled data through numerical calculations is both time-consuming and expensive. In this work, both the PINN and the data-driven neural network are utilized to predict heat conduction in porous media and are subsequently compared to evaluate the prediction efficiency.

### 3.3. Convolutional encoder-decoder neural networks

In Figs. 2 and 3, the convolutional encoder-decoder neural network is composed of two parts: the encoding network and the decoding network. The encoding network is used for down-sampling to capture

the features of the input porous structures and output the high-level coarse feature maps (shown by the gray rectangle in the middle of the network). Subsequently, these high-level coarse feature maps are passed to the decoding network for up-sampling to recover spatial resolution and output the predicted temperature/heat flux fields. Specifically, in the encoding network, the initial input porous structures ( $128 \times 128$  pixels) are fed into the first convolutional layer whose kernel size  $K = 7$ , stride  $s = 2$  and zero padding  $p = 2$  [62]. 48 extracted initial feature maps with reduced sizes ( $64 \times 64$  pixels) are then transferred to a dense block containing multiple densely connected layers. Here, the recently proposed dense block (or DenseNet [63]) is different from the ResNet [64] and Highway Networks [65], which introduces dense connections from any layers to all subsequent layers inside the dense block to boost gradient flow through the network and achieve better parameter efficiency. There are 6, 8 and 6 layers with growth rates of 16 in the three dense blocks, respectively. Each layer includes Batch Normalization (BatchNorm) [66], Rectified Linear Unit (ReLU) [67] and Convolution (or transposed convolution in the decoding network) [62]. The convolution kernel, stride and padding are adjusted to maintain the size of the output feature maps of the dense block to the same size as its input while increasing the number of output feature maps. Next, an encoding layer is applied to reduce both the size and number of outputs for further feature extraction while addressing the explosion in the number of feature maps [62]. Consequently, the resolution of the input images is reduced by 4 times through the encoding network, from  $128 \times 128$  pixels to  $32 \times 32$  pixels. Contrasting with the encoding process, the decoding network is used for up-sampling after passing through the second dense block. The nearest up-sampling method is applied in the decoding layers to avoid the checkerboard effect [40]. Different from the encoding layer, the decoding layer still reduces the number of output feature maps while increasing their size. Finally, the last decoding layer outputs the predicted temperature/heat flux fields with the original spatial resolution of the input porous structure.

In the data-driven neural networks, the loss function is directly calculated according to the MSE Eq. (8)) between the output temperature/heat flux fields and the labeled data. In the case of the PINN, both the output temperature/heat flux fields and their spatial gradients are needed to formulate the physics-informed loss function (Eq. (4-7)). As shown by the green rectangle in Fig. 2, a gradient filter is applied to extract the spatial gradients of the output temperature/heat flux fields. The gradient filter is actually a convolutional layer with designed kernels (see Appendix A for details). The Sobel filter and other filters are commonly utilized in computer vision for feature extraction [68]. Recently, Gao et al. [54] have also developed a gradient filter based on a 4th order central difference scheme. In this work, we design a finite

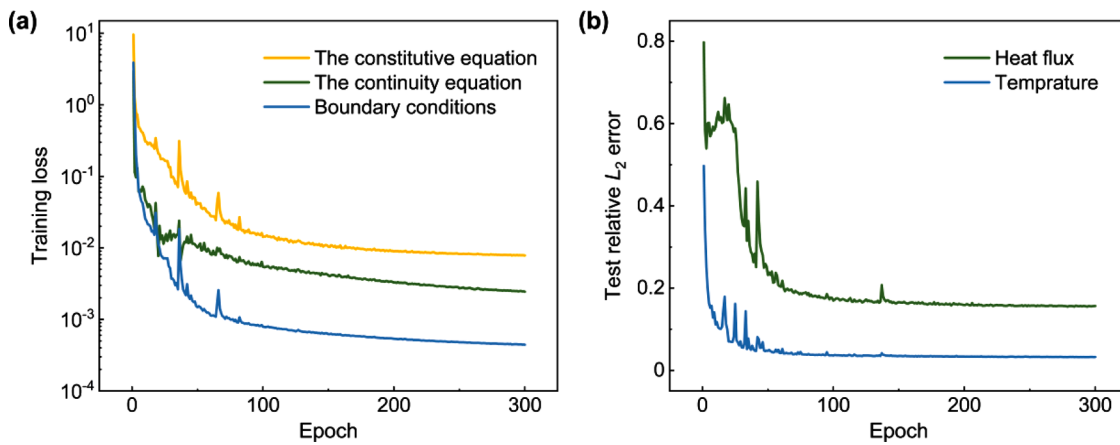


**Fig. 5.** (a) PINN training losses for the constitutive equation (Eq. (6), as shown by the yellow line), the continuity equation (Eq. (5), as shown by the green line), and the boundary conditions (Eq. (7), as shown by the blue line). (b) PINN test relative  $L_2$  errors (Eq. (9)) for the predicted temperature (the blue line) and heat flux (the green line) during the training process.

difference filter to extract horizontal and vertical gradients, which is consistent with the numerical calculations to facilitate fair comparisons (see Appendix A for details).

Next, either the data-driven loss or the physics-informed loss is minimized during the training process. Stochastic gradient descent algorithms using the Adam optimizer are employed to minimize the loss function and train the neural network with an input batch size of 32. A step decay learning rate is applied with an initial learning rate of 0.001, which decays by ten percent every ten epochs. We set a maximum of 300 epochs to ensure adequate training. In order to monitor the training process and evaluate the surrogate performance, test datasets with 512 different porous structures (see Section 3.4 for details) are fed into the neural network at each epoch, using the relative  $L_2$  error as the evaluation metric:

$$L_{2,i} = \frac{1}{M} \sum_{j=1}^M \frac{\|\mathbf{y}_{ij} - \hat{\mathbf{y}}_{ij}\|_2}{\|\hat{\mathbf{y}}_{ij}\|_2}, \quad (9)$$

where  $M = 512$  is the total number of porous structures in the test datasets.  $\hat{\mathbf{y}}_{ij}$  is the surrogate prediction of the  $i$ th output channel for the  $j$ -th porous structure, and  $\mathbf{y}_{ij}$  is the corresponding numerical calculation result. Finally, the trained neural network can be used to predict heat conduction in different porous structures.

### 3.4. Datasets of porous media

The neural network typically requires sufficient training datasets to develop surrogate models (i.e., approximate mathematical models for the outcome of interest to replace complicated computations or measurements) [40]. However, PINNs only necessitate input porous media. Conversely, data-driven neural networks require both the input porous media and the corresponding accurate temperature/heat flux fields as the labeled data. Since the thermophysical characteristics of porous media are determined by multiple factors, including the porosity, pore morphology and pore distribution [36], porous structures with various characteristics should be included in the training datasets to ensure the generalization capability of the neural network. As shown in Fig. 4, we generate a total collection of 20,254 porous structures with various morphologies and stochastic distributions at different porosities ranging from 5% to 60% (5%, 10%, 15%, 20%, 25%, 30%, 35%, 40%, 45%, 50%, 55%, and 60%). All porous structures are generated using the quartet structure generation set (QSGS), a widely applied method that can generate structures closely resembling realistic granular porous media [69]. The porosity, pore size, pore shape and pore distribution can be intentionally controlled in QSGS. These generated porous structures can

actually be regarded as Representative Volume Elements (RVE) that effectively include a sampling of all structural features in the porous media, which are also widely used for predicting effective properties of heterogeneous materials [70,71]. The images of porous structures are set to dimensions of 128 pixels in both length and width for illustrative purposes. Fig. 4(a) shows the effective thermal conductivity of these porous structures calculated from the finite volume method (FVM), where the dimensionless thermal conductivity of the matrix and the pore are set as 1 and 0.1, respectively. The parallel model and series model (dashed lines) give the upper and the lower limits of the effective thermal conductivity at different porosities. Notably, the effective thermal conductivity of the input porous media spans almost the entire range between the upper and lower limits. Fig. 4(b) presents three porous structures, which have decreased effective thermal conductivity with increased porosity  $V_p$ . Fig. 4(c) shows six porous structures with the same porosity ( $V_p = 30\%$ ) and diverse effective thermal conductivity values, which validates the complex relationship between the thermo-physical characteristics of porous media and the interplay of multiple factors.

For the training datasets, a total of 16,384 ( $2^{14}$ ) of all the generated porous structures are randomly chosen as input to train the PINNs. Meanwhile, since we also need to train the data-driven neural networks for comparison with the PINNs, the accurate temperature/heat flux fields of these generated porous structures are prepared as labeled data in the training datasets using numerical calculations. For the test datasets, another set of 512 porous structures from the rest of the generated porous structures are selected to validate the training quality during the training process and evaluate the surrogate performance of the PINNs after training. These porous structures in the test datasets also have porosity ranging from 5% to 60%, while exhibiting different pore morphologies and distributions from those in the training datasets. Isotropic and highly anisotropic porous structures are also included in the test datasets to assess the accuracy and generalizability of surrogate models.

## 4. Results

In this section, we first apply the built PINNs to predict linear heat conduction in porous media. This serves as an illustrative example to demonstrate its accuracy and efficiency through a comparison with numerical calculations and the data-driven neural network. Furthermore, we explore the effectiveness and flexibility of extending the PINNs in addressing more complex problems, demonstrated by predicting nonlinear heat conduction in porous media under large temperature gradients.

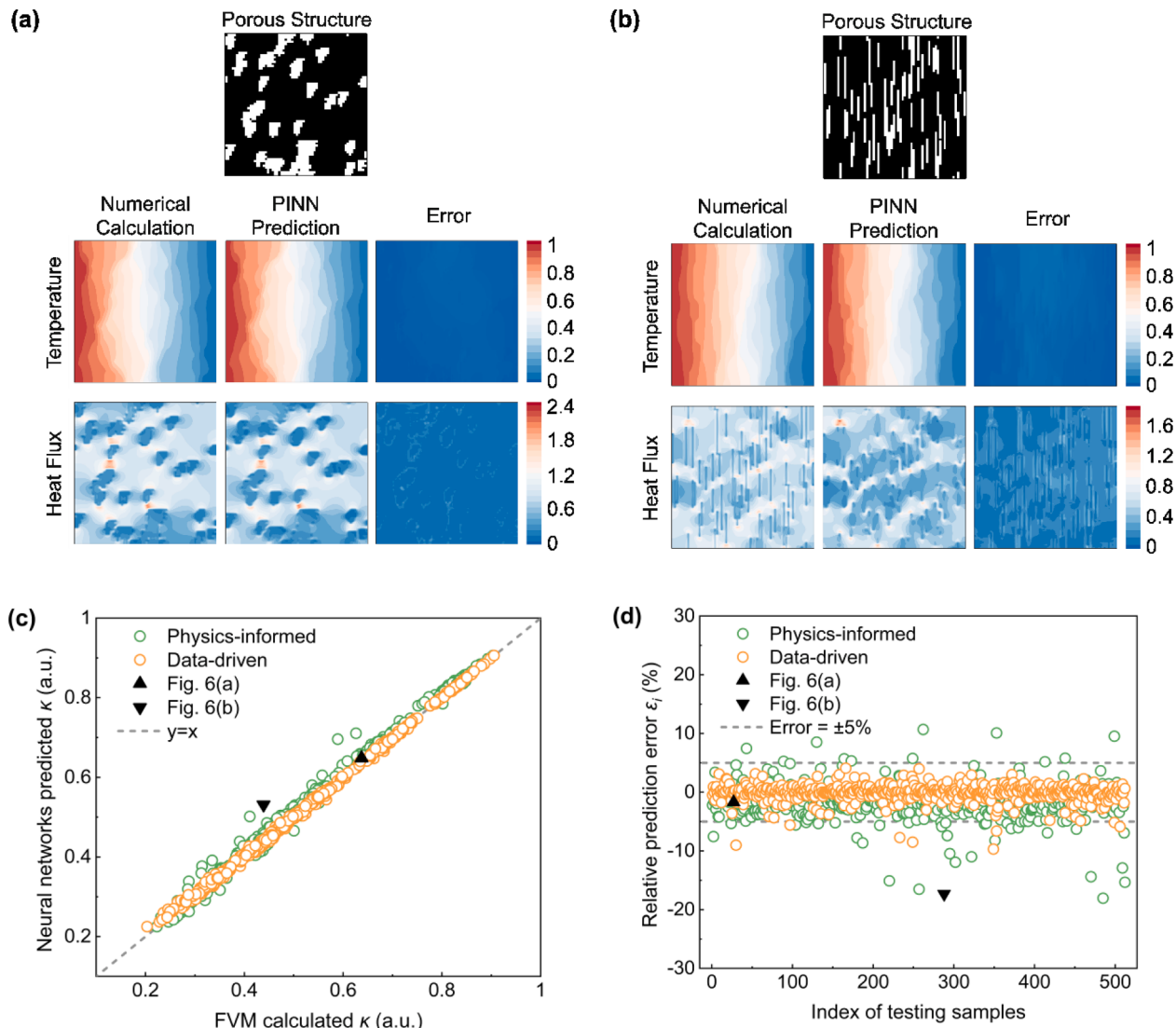


**Fig. 6.** (a-b) Temperature/heat flux fields (in arbitrary units) of two porous media samples in the test dataset. The results from numerical calculations, the PINNs, and the errors between them are shown. (c) The effective thermal conductivity of porous media in test datasets predicted by the PINNs (green symbols) and data-driven neural networks (yellow symbols), in comparison to the FVM calculated results. (d) Relative prediction errors (calculated using Eq. (11)) for the PINNs (green symbols) and data-driven neural networks (yellow symbols). The black triangle symbols represent porous structures shown in (a) and (b).

**Table 1**

The MAPE of temperature/heat flux fields and effective thermal conductivity predicted by PINNs for linear heat conduction in porous media.

Thermophysical characteristics	MAPE (Eqs. (10) and (12))
Temperature fields	5.40%
Heat flux fields	20.6%
Effective thermal conductivity	<b>2.49%</b>

#### 4.1. Linear heat conduction in porous media

We first study linear heat conduction in porous media, where the dimensionless thermal conductivity of the matrix and the pore are constants and are set as 1 and 0.1, respectively, for illustrative purposes. Fig. 5(a) shows the evolution of the physics-informed loss during the training process for each term as defined by Eqs. (5)-(7). Subsequently, Fig. 5(b) shows the test relative  $L_2$  error (Eq. (9)) for the output temperature and heat flux fields. It is notable that both the training loss and the test relative  $L_2$  error converge after the PINN is trained for 300 epochs. Therefore, we can employ the trained neural network to predict

the temperature/heat flux fields of different porous structures, thereby assessing its surrogate performance.

Fig. 6(a) and (b) depict the temperature/heat flux fields of two representative porous media samples from the test dataset. In these figures, we present a comparison between the accurate results calculated from the FVM and the predictions from the trained PINN. For the sample in Fig. 6(a), the PINN demonstrates good accuracy in predicting both the temperature field and the heat flux field. The non-physical checkerboard effect, which generally exists when using conventional gradient filters applied in computer vision [40], is also avoided by applying the finite difference filter. Moreover, the PINN also provides accurate results on the morphology of heat conduction channels within the porous media as shown in the heat flux field, which is useful for analyzing the thermal performance of porous media in engineering [11,12]. However, the predicted heat flux field exhibits relatively larger errors near the junction of the matrix and the pore. This is because the heat flux changes dramatically near the junction, which is difficult to resolve for PINNs [72]. This feature is also reflected in Fig. 5(b), where the test relative  $L_2$  error for the heat flux is larger than that of the temperature. The heat flux prediction errors become more evident for the sample presented in Fig. 6(b), which represents one of the worst cases predicted by the PINNs

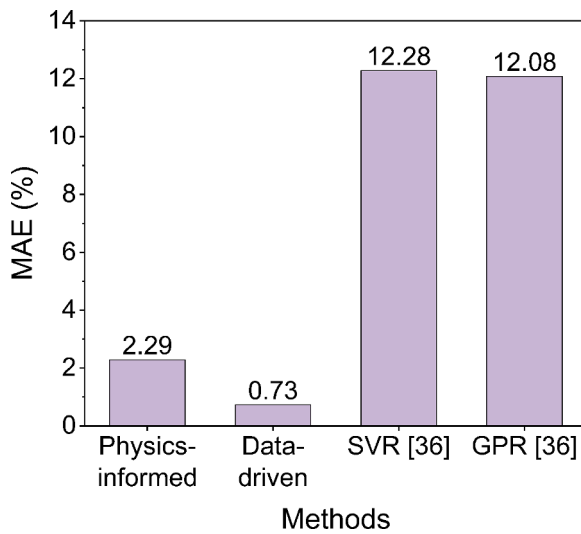


**Fig. 7.** A comparison of the MAE (Eq. (13)) for the effective thermal conductivity predicted by the PINNs, data-driven neural networks and traditional data-driven machine learning methods (SVR and GPR) in the literature [36].

as marked by black triangle symbols in Fig. 6(c) and (d). However, the PINNs still provide relatively accurate temperature field results even in this challenging case. Therefore, the PINN is more capable of predicting the temperature field in porous media than the heat flux field that can also be calculated from the output temperature field using the constitutive equation (Eq. (1)). Further details of the predicted temperature fields with isotherms and heat flux fields with heat flux vectors are given in Appendix B.

Further quantitative evaluations of the prediction accuracy of temperature/heat flux fields are given in Table 1, using the mean absolute percentage error (MAPE) as defined by

$$\text{MAPE} = \frac{1}{M} \frac{1}{n} \sum_j^M \sum_k^n \left| \frac{\hat{y}_{j,k} - y_{j,k}}{y_{j,k}} \right| \times 100\%. \quad (10)$$

Here,  $n$  denotes the total number of uniform grids in a porous media image, and  $M = 512$  denotes the total number of porous structures in the test data;  $\hat{y}_{j,k}$  and  $y_{j,k}$  represent the predicted and accurate temperature/heat flux values for the  $j$ th porous structure in the  $k$ th grid, respectively.

On the other hand, the effective thermal conductivity is also

predicted by PINNs. According to Fourier's law (Eq. (1)), the effective thermal conductivity of the porous media can be obtained from the predicted temperature fields by calculating local temperature gradients (see Appendix B for details). In Fig. 6(c), the effective thermal conductivity of 512 porous structures in the test datasets is compared between the predictions of deep learning neural networks and that calculated from the FVM. It shows that effective thermal conductivity values predicted by PINNs agree well with the FVM calculated values. However, the prediction accuracy is relatively low for porous structures with small effective thermal conductivity. This is due to the fact that these porous structures have narrower heat channels (as shown in Fig. 6(b)), which impose more stringent requirements on the accuracy of temperature/heat flux field predictions.

To quantitatively assess the prediction accuracy of the effective thermal conductivity, we illustrate the relative prediction errors  $\epsilon_j$  with respect to the FVM results in Fig. 6(d), which are defined as

$$\epsilon_j = \frac{\hat{\kappa}_j - \kappa_j}{\kappa_j} \times 100\%, j = 1, 2, \dots, M. \quad (11)$$

The MAPE and the mean absolute error (MAE) can also be examined, which are defined as

$$\text{MAPE} = \frac{1}{M} \sum_j^M |\epsilon_j|, j = 1, 2, \dots, M. \quad (12)$$

$$\text{MAE} = \frac{1}{M} \sum_j^M \left| \frac{\hat{\kappa}_j - \kappa_j}{\bar{\kappa}_j} \right| \times 100\%, j = 1, 2, \dots, M. \quad (13)$$

Here,  $\hat{\kappa}_j$  is the neural network-predicted thermal conductivity for the  $j$ th porous structure in the test dataset, and  $\kappa_j$  is the accurate value calculated by the FVM.  $\bar{\kappa}_j$  is the average value of  $\kappa_j$ . Fig. 6(d) shows that the relative prediction errors of most porous structures are within the range of  $\pm 5\%$ . The calculated MAPE for the PINNs, as listed in Table 1, is

**Table 2**

The MAPE of temperature/heat flux fields and effective thermal conductivity predicted by PINN for nonlinear heat conduction in porous media.

Thermophysical characteristics	MAPE (Eqs. (10) and (12))
Temperature fields	4.50%
Heat flux fields	14.4%
Effective thermal conductivity	2.73%

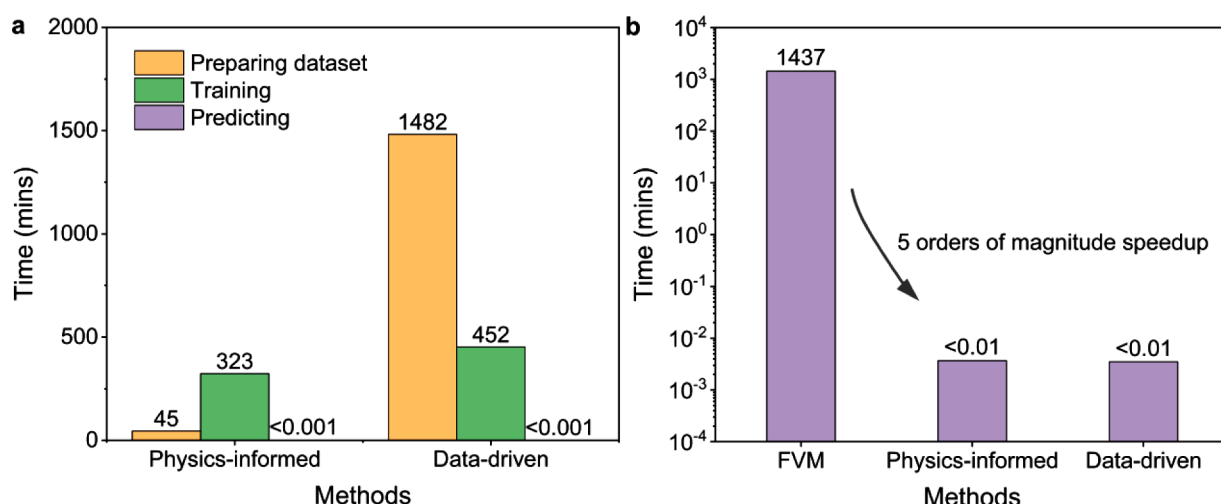


**Fig. 8.** (a) The time required for developing surrogate models using the PINNs and data-driven neural networks, including the time required for preparing the datasets, training the neural network, and predicting heat conduction in 512 porous media samples in the test dataset. (b) The time required for predicting heat conduction in 16,384 porous media samples using neural networks and numerical calculations.

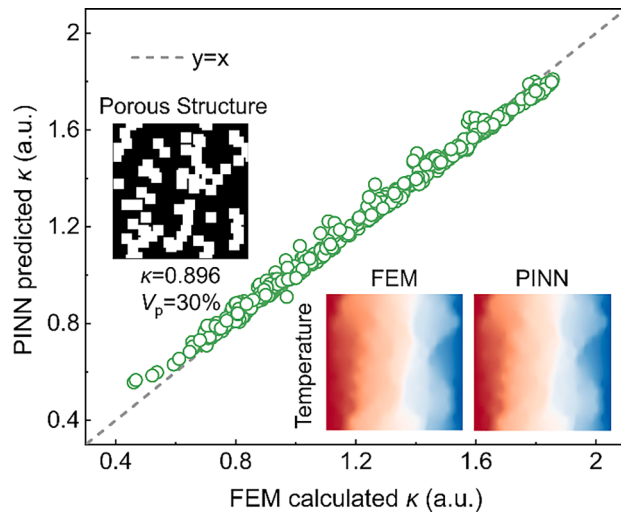


**Fig. 9.** The effective thermal conductivity of nonlinear heat conduction in the porous media of the test datasets predicted by PINNs and the FEM. The inset provides a comparison of temperature fields for a porous media sample, illustrating results obtained from both the FEM and the PINNs.

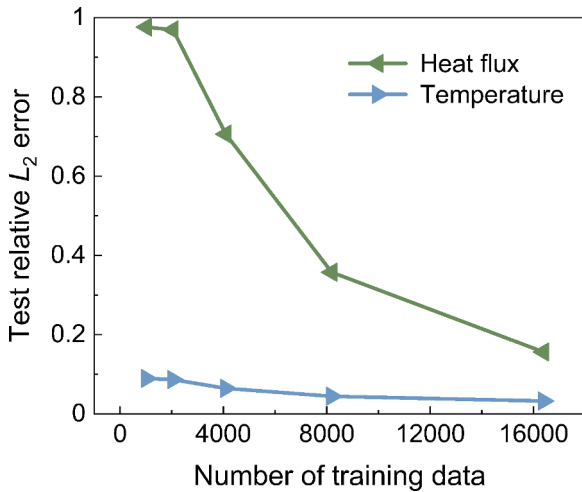


**Fig. 10.** The test relative  $L_2$  error (Eq. (9)) of the predicted temperature (the blue line) and heat flux (the green line) for the PINN trained with different numbers of porous structures after 300 epochs.

2.49%, which is accurate enough for engineering applications. Meanwhile, the results predicted by the data-driven neural networks are also plotted for comparison (yellow symbols in Fig. 6(c-d)). The calculated MAPE for data-driven neural networks is 0.93%. Therefore, PINNs provide a comparable surrogate performance to state-of-the-art data-driven neural networks.

When compared with traditional data-driven machine learning methods, such as the support vector regression (SVR) and Gaussian process regression (GPR), which have been shown to exhibit average relative prediction errors larger than 10% in previous investigations as shown in Fig. 7 [36], the prediction accuracy for the effective thermal conductivity has been significantly improved by the PINNs.

In addition to the prediction accuracy of the temperature/heat flux fields and the effective thermal conductivity, we also examine the time required for developing the surrogate model to evaluate the efficiency of the PINNs. Fig. 8(a) presents the total time required for developing surrogate models using PINNs and data-driven neural networks. This includes the time required for preparing the datasets using the FVM, training the neural network, and predicting heat conduction in 512

porous media samples from the test dataset. It is worth noting that both the PINNs and data-driven neural networks are trained for 300 epochs, and the allocated computing resources are also the same (see Appendix C for more details). The results reveal that PINNs require significantly less time than data-driven neural networks since no labeled training data is needed. The time costs associated with training PINNs and data-driven neural networks are comparable. After the training process, the computational speeds of the trained neural networks and case-by-case numerical calculations are also compared as shown in Fig. 8(b). For the 16,384 porous media samples in the training dataset, both the PINNs and the data-driven neural networks achieve speedups up to 5 orders of magnitude over numerical calculations. It's important to note that the speedup also depends on the computational capabilities. Consequently, without the requirement for labeled training data, the PINNs demonstrate good prediction accuracy for linear heat conduction in porous media with significantly reduced time cost compared to both data-driven neural networks and numerical calculations.

#### 4.2. Nonlinear heat conduction in porous media

Furthermore, as a case study, we also explore the ability of the built PINN in solving more complex physical problems, particularly focusing on nonlinear heat conduction in porous media. Porous media are commonly applied in working conditions with large temperature gradients in engineering, such as thermal barrier coatings in aeronautics [73]. In such situations, the thermal conductivity values of both the matrix and the pore are not constants, and change with the temperature as shown in Eqs. (1) and (2). Solving this nonlinear heat conduction problem introduces increased numerical iterations and considerable computational resources when using numerical calculations, and also requires re-preparing the labeled training data when using data-driven machine learning methods [25]. In this context, we extend the PINNs shown in Fig. 2 to predict nonlinear heat conduction in porous media by modifying the physics-informed loss function according to the governing equations (Eqs. (1) and (2)) and boundary conditions (Eq. (3)). The temperature-dependent thermal conductivity in Eqs. (1) and (2) take the form of  $\kappa(T) = \kappa_0(1 + \alpha T)$ , which is widely adopted in engineering [74, 75]. We set  $\kappa_0$  as 1 and 0.1 for the matrix and the pore, respectively, while  $\alpha$  is set as 2 for both phases for illustrative purposes. The same input of 16,384 porous media samples is employed as the training dataset without any labeled data. Accurate temperature/heat flux fields of 512 samples in the test datasets are prepared using the finite element method (FEM) [76]. The PINNs are trained to converge within 300 epochs. As shown in Table 2, for nonlinear heat conduction in porous media, the PINNs provide a good surrogate accuracy in predicting temperature/heat flux fields. Additionally, we compare the effective thermal conductivity predicted by the PINNs with the results obtained from numerical calculations in Fig. 9. Again, the predicted effective thermal conductivity matches well with the FEM results, yielding a MAPE of 2.73% as listed in Table 2. Meanwhile, for numerical calculations, the time required for predicting nonlinear heat conduction in 16,384 porous media samples of the training datasets is 2861 min, still within the same order of magnitude as that of the linear heat conduction problem. In contrast, the PINNs' time required for training and predicting remains comparable to that of the linear heat conduction problem since the architecture of neural networks and training epochs are the same, which maintains a 5-orders-of-magnitude speedup over numerical calculations. Therefore, the PINN can efficiently predict nonlinear heat conduction in porous media, while also showcasing significant potential for solving other complex physical problems. This is accomplished by simply changing the loss function formulas according to physical governing equations, which is impractical for data-driven machine learning methods and traditional numerical calculations.

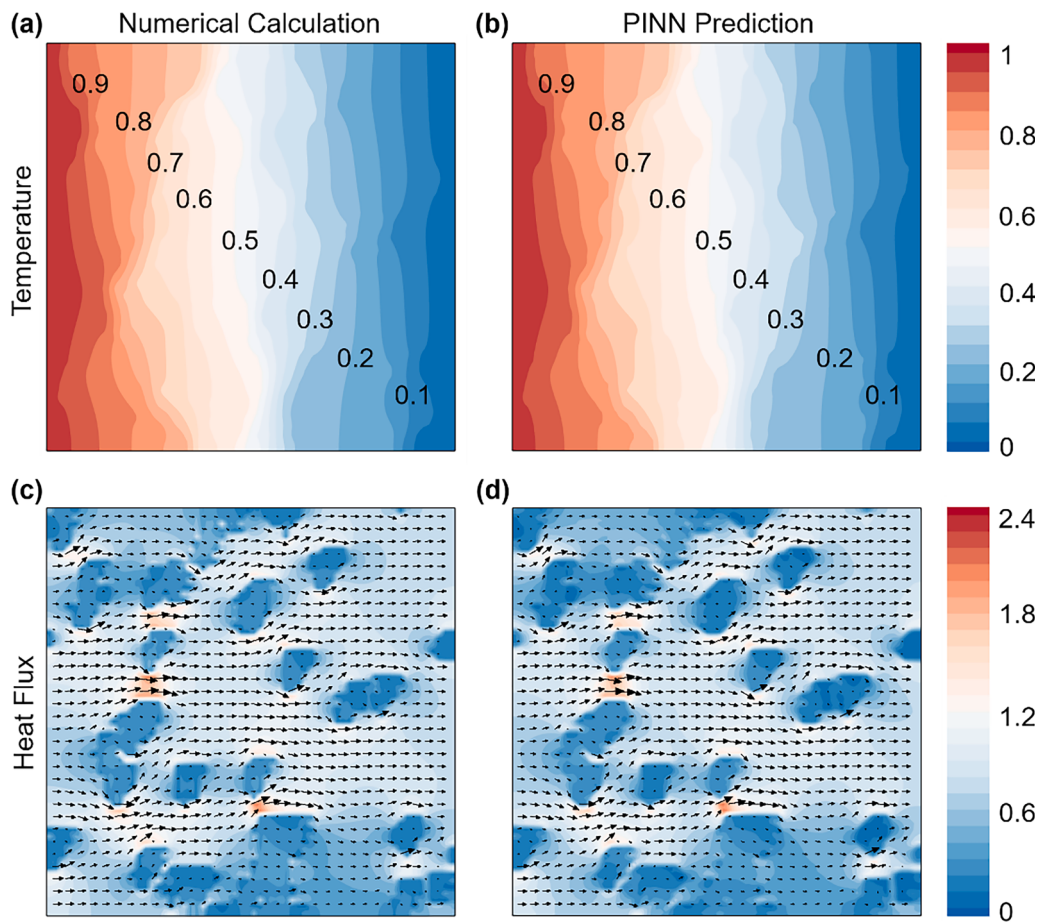


**Fig. B1.** Temperature distributions with isotherms and heat flux distributions with heat flux vectors obtained from (a) numerical calculations and (b) PINN predictions for a porous media sample with accurate prediction results. The size and length of the black arrows in heat flux distributions represent the magnitude of the local heat flux, while the direction of the arrows indicate the direction of the local heat flux.

## 5. Discussions

### 5.1. Impact of hyperparameters and datasets on the learning performance

In this work, the convolutional encoder-decoder neural network employed is a standard architecture commonly used for image-to-image regression tasks when dense pixel-wise predictions are required [77]. As shown in Fig. 2 and introduced in Section 3.3, the architecture of the convolutional encoder-decoder neural network is elaborately designed for surrogate modeling of physical systems governed by partial differential equations with high-dimensional inputs, utilizing advances developed in computer vision [63]. The fully connected layers in traditional CNNs have been replaced with a convolutional layer at the end of the decoder to recover the input's spatial resolution, enabling the network to output physical fields in the real spatial domain. Meanwhile, in contrast to the Unet [59] and the Segnet [60] in computer vision, recently proposed DenseNets [63] are applied to increase connectivity within and between down-sampling (the encoder) and up-sampling (the decoder) paths [62]. This strategy enhances gradient flow through the neural network, enabling it to learn solutions to complex physical problems with various inputs (e.g., porous structures with various morphologies and stochastic distributions at different porosities). The architecture details of the convolutional encoder-decoder neural networks, including the spatial resolution of feature maps during down-sampling, kernels of convolution layers, number of layers, and growth rate in dense blocks, have been optimized in both this study and the literature [62]. Training hyperparameters, including the total number of epochs, batch size, learning rate, and weight coefficients for

each governing equation in the physics-informed loss, have also been carefully searched to achieve better surrogate performance. As shown in Fig. 5, the PINNs already start to converge after training for 200 epochs, and we stop training after 300 epochs for the sake of caution. The initial learning rate is set to 0.001 which decays by ten percent every ten epochs. Our results have indicated that further changes in the initial learning rates, decay rates, or learning rate scheduler strategies lead to reduced training performance. A batch size of 32 is recommended, as larger batch sizes (e.g., 48) diminish the efficacy of the trained neural network, while smaller batch sizes (e.g., 16) fail to provide improved surrogate performance but significantly prolong the training duration. Among the hyperparameters considered, the weight coefficients for each governing equation in the physics-informed loss ( $\lambda_1$ ,  $\lambda_2$  and  $\lambda_3$  for the constitutive equation, the continuity equation, and the boundary conditions respectively, as given in Eqs. (4)-(7)) exert the most significant impact on the surrogate performance of the PINNs. After multiple attempts, the three weight coefficients are chosen as 10, 1 and 1, respectively. We set a large weight coefficient for the constitutive equation that constrains the relation between temperature and heat flux. This is because the PINN has been shown to be more capable of predicting the temperature field in porous structures than the heat flux field in Fig. 5. By elevating the weight coefficient for the constitutive equation, the training of neural networks is forced to output heat flux that is consistent with the more accurately predicted temperature values, leading to improved predictions for the heat flux field in porous structures. It is worth noting that further enhancements in the accuracy of heat flux predictions can potentially be achieved through developing novel strategies that precisely tune the tricky balance among multiple

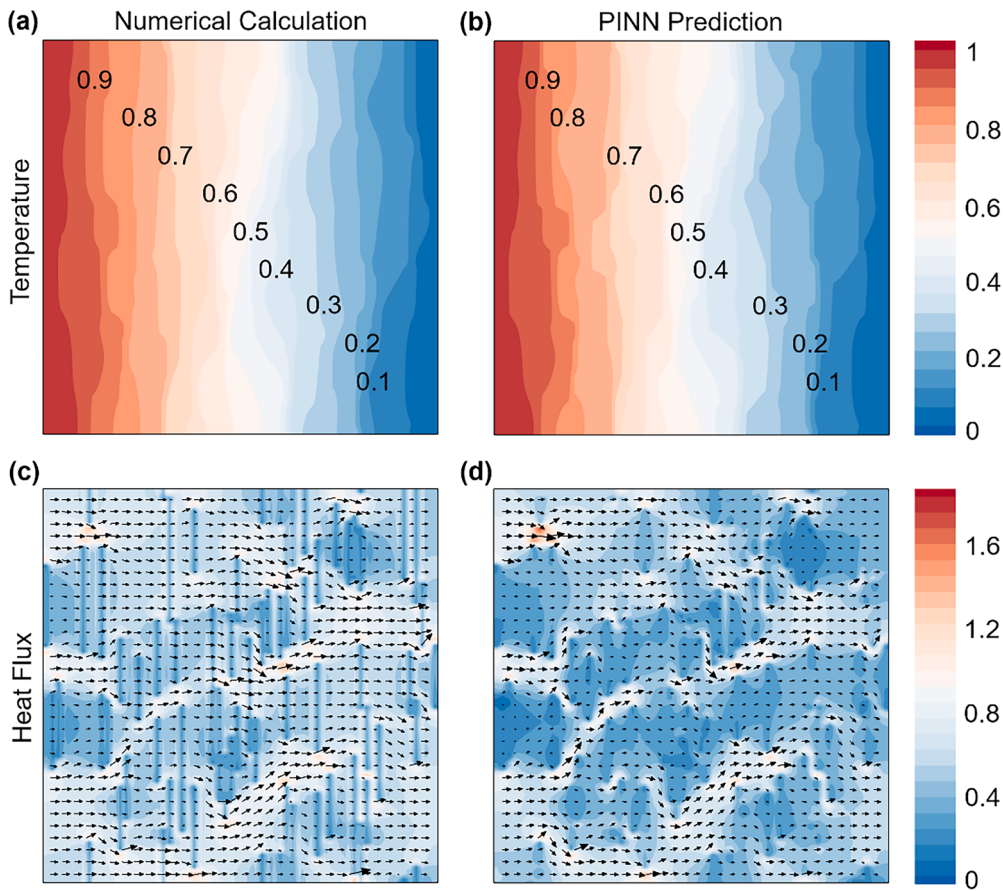


**Fig. B2.** Temperature distributions with isotherms and heat flux distributions with heat flux vectors from (a) numerical calculations and (b) PINN predictions for a porous media sample with relatively worse prediction results.

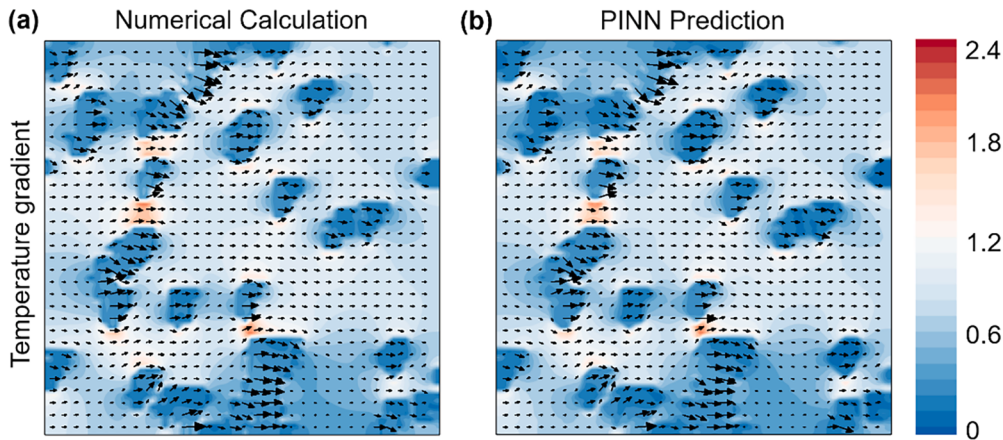


**Fig. B3.** Temperature gradient distributions with temperature gradient flux vectors from (a) numerical calculations and (b) PINN predictions for a porous media sample with accurate prediction results. The size and length of the black arrows represent the magnitude of the local temperature gradient, while the direction of the arrows represent the direction of the local temperature gradient.

physics-informed loss terms [78,79].

In addition, we have also investigated the impact of the datasets utilized in this work. We trained the PINNs with varying quantities of porous structures in the training dataset and examined their effect on surrogate performance. Fig. 10 shows the test relative  $L_2$  errors for the neural network after 300 training epochs. A clear trend towards convergence is observed for both the temperature and heat flux fields. Increasing the number of porous structures used for training the PINN consistently leads to improved surrogate performance, which is

convenient since no labeled data is required. In previous sections, we have presented predicted results using 16,384 ( $2^{14}$ ) porous structures as the training datasets as representative examples. Furthermore, it is worth noting that the generated porous structures in this work exhibit various morphologies, ranging from pure isotropic (with an approximate circular shape as porous structure 5 in Fig. 4) to highly anisotropic pores (represented by porous structures 7 and 9 in Fig. 4). Higher prediction accuracy can be achieved when only isotropic porous structures are considered [35].

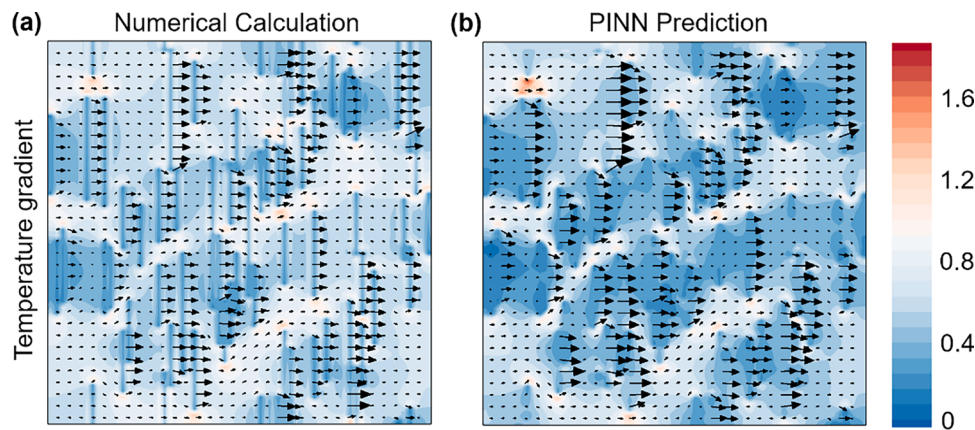


**Fig. B4.** Temperature gradient distributions with temperature gradient flux vectors from (a) numerical calculations and (b) PINN predictions for a porous media sample with relatively worse prediction results.

### 5.2. Potential of the current framework

The most prominent advantage of the proposed PINNs in this work is its labeled-data-free feature. Preparing the labeled training data (accurate temperature/heat flux fields for all the porous structures in the training dataset from numerical calculations), which is very time-consuming as shown in Fig. 8, is not needed. This allows the PINNs built for predicting linear heat conduction in porous media to be directly applied to solve nonlinear heat conduction problems by simply changing the formulas of physics-informed loss using the governing equations, as we already demonstrated in Section 4.2. In principle, the current framework can also be extended to solve other complex physics problems in porous media or material systems, such as the Darcy flow in porous permeable media [40] and the directional Young's modulus of porous materials under normal compressional force [29]. It is worth noting that additional efforts are needed to optimize the architecture and hyperparameters of the neural network to achieve good surrogate performance, depending on the complexity of the problem, especially for multiphase flow problems in porous media [80,81]. Moreover, further attempts can be undertaken to extend the current PINN to predict heat transfer in real three-dimensional (3D) porous structures, such as using 3D convolutional neural networks and taking multiple connected cross-section images of 3D porous structures as input to train 2D convolutional neural networks [13].

### 6. Summary

In summary, we have employed the PINN to investigate heat conduction problems in various porous media. In the absence of labeled data, granular porous structures including a wide range of porosity and various pore distributions and morphologies, are used to train a physics-informed convolutional encoder-decoder neural network. The trained PINN provides a good surrogate performance in predicting temperature/heat flux fields in various porous media. The extracted effective thermal conductivity also shows good accuracy when compared with numerical calculation results, with an average relative prediction error of 2.49%. On the other hand, the PINN requires significantly less time to develop surrogate models than data-driven neural networks since no labeled data are required, and also achieves a speedup of up to 5 orders of

magnitude in prediction over numerical calculations. Furthermore, taking nonlinear heat conduction in porous media as an example, we demonstrate that the PINN possesses good flexibility in resolving more complex physical problems by simply adjusting the loss function according to governing physical equations, which is beyond the reach of data-driven machine learning methods and traditional numerical calculations. The proposed PINN in this work holds significant promise for the analysis and optimization of heat transfer in practical applications, such as thermal radiation and heat convection coupled with heat conduction in porous media.

### CRediT authorship contribution statement

**Jiaxuan Xu:** Methodology, Data curation, Investigation, Writing – original draft, Visualization. **Han Wei:** Methodology, Data curation. **Hua Bao:** Conceptualization, Writing – review & editing, Supervision.

### Declaration of Competing Interest

The authors declare that they have no known competing financial interests or personal relationships that could have appeared to influence the work reported in this paper.

### Data availability

The PINN models and data that support the findings of this study are openly available to download from [https://github.com/JoshuaXu7/PINN\\_porous](https://github.com/JoshuaXu7/PINN_porous) upon publication.

### Acknowledgments

J.X., H.W., and H.B. acknowledge the support by the National Key R & D Project from Ministry of Science and Technology of China (Grant No. 2022YFA1203100) and the National Natural Science Foundation of China (Grant No. 52122606). Simulations were performed on the  $\pi$  2.0 cluster and the Siyuan Mark-I cluster supported by the Center for High Performance Computing at Shanghai Jiao Tong University.

### Appendix A. Gradient filters

According to the governing equations Eq. (1)-(2), it is necessary to extract spatial gradients of the output temperature/heat flux fields from encoder-decoder neural networks in order to construct the physics-informed loss function. For consistency with numerical calculations that utilize the central difference scheme, the finite difference filter is applied to estimate horizontal and vertical spatial gradients:

$$\mathcal{H} = \begin{bmatrix} 0 & 0 & 0 \\ -1 & 0 & 1 \\ 0 & 0 & 0 \end{bmatrix}, \quad \mathcal{V} = \begin{bmatrix} 0 & 1 & 0 \\ 0 & 0 & 0 \\ 0 & -1 & 0 \end{bmatrix}. \quad (\text{A1})$$

We note that gradient filters are implemented as  $3 \times 3$  kernels in a convolutional layer, as shown by the green rectangle in Fig. 2. Therefore, when temperature/heat flux fields are fed to this convolutional layer and subjected to convolutional calculations using the gradient filters as kernels, the output of the convolutional layer corresponds to the spatial temperature/heat flux gradients.

The forward difference method is applied at the boundary using a correction matrix and a replicate padding. For 2D image matrix  $\mathbf{I}$  and horizontal gradient kernel  $\mathcal{H}$ , the correction matrix  $M_{\mathcal{H}}$  is given by:

$$M_{\mathcal{H}} = \begin{bmatrix} 2 & 0 & 0 \\ 0 & 1 & \ddots \\ 0 & & 1 & 0 \\ 0 & 0 & 2 \end{bmatrix}. \quad (\text{A2})$$

Subsequently, the horizontal gradient can be estimated as  $(\mathbf{I} * \mathcal{H})M_{\mathcal{H}}$ , where  $*$  donates the convolution operator. This convolution operation can be seamlessly integrated into convolutional neural networks. The correction of the vertical gradient at the boundary is similar to that of the horizontal gradient. Our results demonstrate that the finite difference filter provides high prediction accuracy and effectively mitigates the checkerboard effect that is often encountered when conventional gradient filters, such as the Sobel filter [68], are used in computer vision.

## Appendix B. Details of examples of PINNs prediction results

To provide more details of the PINN prediction results, as presented in Fig. 6 of the main text, we show temperature distributions using isotherms and heat flux distributions with heat flux vectors in Figs. B1 and B2. Both the sample with accurate prediction results (Fig. B1) and the sample with relatively worse prediction results (Fig. B2) are given.

Additionally, temperature gradient distributions with temperature gradient vectors are also provided as shown in Figs. B3 and B4. After multiplying these temperature gradients with the corresponding thermal conductivity of the pore or matrix, the effective thermal conductivity of the porous media can be calculated.

## Appendix C. Computation resources

The algorithms for deep learning neural networks are implemented using the PyTorch platform [82]. The training and testing of both PINNs and data-driven neural networks are performed on 2 NVIDIA Tesla V100 Graphic Processing Units (GPU). The FEM calculations utilize the FEniCSx, a popular open-source computing platform for solving partial differential equations (PDEs) [76]. The FVM calculations utilize our in-house code. The FVM and FEM calculations are executed on 10 Intel Xeon ICX Platinum 8358 Central Processing Units (CPU). The time required for developing deep learning surrogate models depends on the allocated computation resources.

## References

- [1] R. Vaßen, M.O. Jarligo, T. Steinke, D.E. Mack, D. Stöver, Overview on advanced thermal barrier coatings, *Surf. Coat. Technol.* 205 (4) (2010) 938–942.
- [2] Q. Wang, X.H. Han, A. Sommers, Y. Park, C. T' Joen, A. Jacobi, A review on application of carbonaceous materials and carbon matrix composites for heat exchangers and heat sinks, *Int. J. Refrig.* 35 (1) (2012) 7–26.
- [3] L. Yang, D. Huh, R. Ning, V. Rapp, Y. Zeng, Y. Liu, S. Ju, Y. Tao, Y. Jiang, J. Beak, J. Leem, S. Kaur, H. Lee, X. Zheng, R.S. Prasher, High thermoelectric figure of merit of porous Si nanowires from 300 to 700 K, *Nat. Commun.* 12 (1) (2021) 3926.
- [4] L. Xu, J. Liu, P. Jin, G. Xu, J. Li, X. Ouyang, Y. Li, C.W. Qiu, J. Huang, Black-hole-inspired thermal trapping with graded heat-conduction metadevices, *Natl. Sci. Rev.* 10 (2) (2022) nwac159.
- [5] L. Xu, G. Xu, J. Huang, C.W. Qiu, Diffusive Fizeau drag in spatiotemporal thermal metamaterials, *Phys. Rev. Lett.* 128 (14) (2022), 145901.
- [6] L. Xu, J. Liu, G. Xu, J. Huang, C.W. Qiu, Giant, magnet-free, and room-temperature Hall-like heat transfer, *Proc. Natl. Acad. Sci.* 120 (27) (2023), e2305755120.
- [7] G.L. Vignoles, A. Ortona, Numerical study of effective heat conductivities of foams by coupled conduction and radiation, *Int. J. Therm. Sci.* 109 (2016) 270–278.
- [8] G. Peng, S.W. Sharshir, Y. Wang, M. An, D. Ma, J. Zang, A.E. Kabeel, N. Yang, Potential and challenges of improving solar still by micro/nano-particles and porous materials - a review, *J. Clean. Prod.* 311 (2021), 127432.
- [9] T. Xie, Y.-L. He, Z.J. Hu, Theoretical study on thermal conductivities of silica aerogel composite insulating material, *Int. J. Heat Mass Transf.* 58 (1) (2013) 540–552.
- [10] G. Xu, J.M. LaManna, J.T. Clement, M.M. Mench, Direct measurement of through-plane thermal conductivity of partially saturated fuel cell diffusion media, *J. Power Sources* 256 (2014) 212–219.
- [11] Y. Wang, H. Liu, X. Ling, Y. Weng, Effects of pore microstructure on the effective thermal conductivity of thermal barrier coatings, *Appl. Therm. Eng.* 102 (2016) 234–242.
- [12] F. Sun, X. Fan, T. Zhang, P. Jiang, J. Yang, Numerical analysis of the influence of pore microstructure on thermal conductivity and Young's modulus of thermal barrier coating, *Ceram. Int.* 46 (15) (2020) 24326–24332.
- [13] Q. Rong, H. Wei, X. Huang, H. Bao, Predicting the effective thermal conductivity of composites from cross sections images using deep learning methods, *Compos. Sci. Technol.* 184 (2019), 107861.
- [14] H. Zhao, Z. Ning, Q. Kang, L. Chen, T. Zhao, Relative permeability of two immiscible fluids flowing through porous media determined by lattice Boltzmann method, *Int. Commun. Heat Mass Transfer* 85 (2017) 53–61.
- [15] X. Zhu, S. Wang, Q. Feng, L. Zhang, L. Chen, W. Tao, Pore-scale numerical prediction of three-phase relative permeability in porous media using the lattice Boltzmann method, *Int. Commun. Heat Mass Transfer* 126 (2021), 105403.
- [16] H. Wei, H. Bao, X. Ruan, Perspective: predicting and optimizing thermal transport properties with machine learning methods, *Energy AI* 8 (2022), 100153.
- [17] J.P. Arenas, M.J. Crocker, Recent trends in porous sound-absorbing materials, *Sound Vib.* 44 (7) (2010) 12–18.
- [18] M.A.B. Zanoni, J.L. Torero, J.I. Gerhard, Determination of the interfacial heat transfer coefficient between forced air and sand at Reynold's numbers relevant to smouldering combustion, *Int. J. Heat Mass Transf.* 114 (2017) 90–104.
- [19] D.A.G. Bruggeman, Berechnung verschiedener physikalischer Konstanten von heterogenen Substanzen. III. Die elastischen Konstanten der quasiiotropen Mischkörper aus isotropen Substanzen, *Ann. Phys.* 421 (2) (1937) 160–178.
- [20] D.P.H. Hasselman, L.F. Johnson, Effective thermal conductivity of composites with interfacial thermal barrier resistance, *J. Compos. Mater.* 21 (6) (1987) 508–515.
- [21] M.J. Sailor, Chemistry of porous silicon, *Porous Silicon in Practice* (2011) 189–227.
- [22] J. Ma, C. Nan, Effective-medium approach to thermal conductivity of heterogeneous materials, *Annu. Rev. Heat Transfer* 17 (2014).
- [23] M. Varmazyan, M. Bazargan, Development of a thermal lattice Boltzmann method to simulate heat transfer problems with variable thermal conductivity, *Int. J. Heat Mass Transf.* 59 (2013) 363–371.
- [24] C. Demuth, M.A.A. Mendes, S. Ray, D. Trimis, Performance of thermal lattice Boltzmann and finite volume methods for the solution of heat conduction equation in 2D and 3D composite media with inclined and curved interfaces, *Int. J. Heat Mass Transf.* 77 (2014) 979–994.
- [25] P. Zhu, L.W. Zhang, K.M. Liew, Geometrically nonlinear thermomechanical analysis of moderately thick functionally graded plates using a local Petrov–Galerkin approach with moving Kriging interpolation, *Compos. Struct.* 107 (2014) 298–314.

- [26] M. Mierzwiczak, W. Chen, Z.J. Fu, The singular boundary method for steady-state nonlinear heat conduction problem with temperature-dependent thermal conductivity, *Int. J. Heat Mass Transf.* 91 (2015) 205–217.
- [27] Z. Tong, M. Liu, H. Bao, A numerical investigation on the heat conduction in high filler loading particulate composites, *Int. J. Heat Mass Transf.* 100 (2016) 355–361.
- [28] Y. Hu, Y. Shen, H. Bao, Ultra-efficient and parameter-free computation of submicron thermal transport with phonon Boltzmann transport equation, *Fund. Res.* (2022).
- [29] A. Rabbani, M. Babaei, R. Shams, Y.D. Wang, T. Chung, DeePore: a deep learning workflow for rapid and comprehensive characterization of porous materials, *Adv. Water Resour.* 146 (2020), 103787.
- [30] J.E. Santos, D. Xu, H. Jo, C.J. Landry, M. Prodanović, M.J. Pyrcz, PoreFlow-Net: a 3D convolutional neural network to predict fluid flow through porous media, *Adv. Water Resour.* 138 (2020), 103539.
- [31] J. Wan, J.W. Jiang, H.S. Park, Machine learning-based design of porous graphene with low thermal conductivity, *Carbon* 157 (2020) 262–269.
- [32] H. Wang, Y. Yin, X.Y. Hui, J.Q. Bai, Z.G. Qu, Prediction of effective diffusivity of porous media using deep learning method based on sample structure information self-amplification, *Energy AI* 2 (2020), 100035.
- [33] W. Fei, G.A. Narsilio, M.M. Disfani, Predicting effective thermal conductivity in sands using an artificial neural network with multiscale microstructural parameters, *Int. J. Heat Mass Transf.* 170 (2021), 120997.
- [34] S.M. Arifuzzaman, K. Dong, H. Zhu, Q. Zeng, DEM study and machine learning model of particle percolation under vibration, *Adv. Powder Technol.* 33 (5) (2022), 103551.
- [35] H. Wei, S. Zhao, Q. Rong, H. Bao, Predicting the effective thermal conductivities of composite materials and porous media by machine learning methods, *Int. J. Heat Mass Transf.* 127 (2018) 908–916.
- [36] H. Wei, H. Bao, X. Ruan, Machine learning prediction of thermal transport in porous media with physics-based descriptors, *Int. J. Heat Mass Transf.* 160 (2020), 120176.
- [37] H. Wei, H. Bao, X. Ruan, Genetic algorithm-driven discovery of unexpected thermal conductivity enhancement by disorder, *Nano Energy* 71 (2020), 104619.
- [38] M. Wang, H. Wang, Y. Yin, S. Rahardja, Z. Qu, Temperature field prediction for various porous media considering variable boundary conditions using deep learning method, *Int. Commun. Heat Mass Transfer* 132 (2022), 105916.
- [39] L. Gondara, Medical image denoising using convolutional denoising autoencoders, in: 2016 IEEE 16th International Conference on Data Mining Workshops (ICDMW), 2016, pp. 241–246.
- [40] Y. Zhu, N. Zabaras, P.S. Koutsourelakis, P. Perdikaris, Physics-constrained deep learning for high-dimensional surrogate modeling and uncertainty quantification without labeled data, *J. Comput. Phys.* 394 (2019) 56–81.
- [41] L. Sun, H. Gao, S. Pan, J.X. Wang, Surrogate modeling for fluid flows based on physics-constrained deep learning without simulation data, *Comput. Methods Appl. Mech. Eng.* 361 (2020), 112732.
- [42] M. Raissi, P. Perdikaris, G.E. Karniadakis, Physics-informed neural networks: a deep learning framework for solving forward and inverse problems involving nonlinear partial differential equations, *J. Comput. Phys.* 378 (2019) 686–707.
- [43] N. Geneva, N. Zabaras, Modeling the dynamics of PDE systems with physics-constrained deep auto-regressive networks, *J. Comput. Phys.* 403 (2020), 109056.
- [44] R. Li, J.X. Wang, E. Lee, T. Luo, Physics-informed deep learning for solving phonon Boltzmann transport equation with large temperature non-equilibrium, *npj Comput. Mater.* 8 (1) (2022) 29.
- [45] B. Bahmani, W. Sun, Training multi-objective/multi-task collocation physics-informed neural network with student/teachers transfer learnings, arXiv preprint arXiv:2107.11496, (2021).
- [46] Z. Fang, A high-efficient hybrid physics-informed neural networks based on convolutional neural network, *IEEE Trans. Neural Netw. Learn. Syst.* 33 (10) (2022) 5514–5526.
- [47] Y. Chen, L. Lu, G.E. Karniadakis, L. Dal Negro, Physics-informed neural networks for inverse problems in nano-optics and metamaterials, *Opt. Express* 28 (8) (2020) 11618–11633.
- [48] M. Raissi, A. Yazdani, G.E. Karniadakis, Hidden fluid mechanics: learning velocity and pressure fields from flow visualizations, *Science* 367 (6481) (2020) 1026–1030.
- [49] H. Cavanagh, A. Mosbach, G. Scalliet, R. Lind, R.G. Endres, Physics-informed deep learning characterizes morphodynamics of Asian soybean rust disease, *Nat. Commun.* 12 (1) (2021) 6424.
- [50] G.E. Karniadakis, I.G. Kevrekidis, L. Lu, P. Perdikaris, S. Wang, L. Yang, Physics-informed machine learning, *Nat. Rev. Phys.* 3 (6) (2021) 422–440.
- [51] R. Li, E. Lee, T. Luo, Physics-informed neural networks for solving multiscale mode-resolved phonon Boltzmann transport equation, *Mater. Today Phys.* 19 (2021), 100429.
- [52] L. Lu, P. Jin, G. Pang, Z. Zhang, G.E. Karniadakis, Learning nonlinear operators via DeepONet based on the universal approximation theorem of operators, *Nature Mach. Intell.* 3 (3) (2021) 218–229.
- [53] S.M. Arifuzzaman, K. Dong, A. Yu, Process model of vibrating screen based on DEM and physics-informed machine learning, *Powder Technol.* 410 (2022), 117869.
- [54] H. Gao, L. Sun, J.X. Wang, PhyGeoNet: physics-informed geometry-adaptive convolutional neural networks for solving parameterized steady-state PDEs on irregular domain, *J. Comput. Phys.* 428 (2021), 110079.
- [55] C.G. Fraces, H. Tchelepi, Physics informed deep learning for flow and transport in porous media, in: SPE Reservoir Simulation Conference, 2021. D011S006R002.
- [56] K. Wang, Y. Chen, M. Mehana, N. Lubbers, K.C. Bennett, Q. Kang, H. S. Viswanathan, T.C. Germann, A physics-informed and hierarchically regularized data-driven model for predicting fluid flow through porous media, *J. Comput. Phys.* 443 (2021), 110526.
- [57] F.P. Incropera, D.P. DeWitt, T.L. Bergman, A.S. Lavine, *Fundamentals of Heat and Mass Transfer*, Wiley, New York, 1996.
- [58] N. Lubbers, T. Lookman, K. Barros, Inferring low-dimensional microstructure representations using convolutional neural networks, *Phys. Rev. E* 96 (5) (2017), 052111.
- [59] O. Ronneberger, P. Fischer, T. Brox, U-Net: convolutional networks for biomedical image segmentation, in: International Conference on Medical Image Computing and Computer-Assisted Intervention, Springer, 2015, pp. 234–241.
- [60] V. Badrinarayanan, A. Kendall, R. Cipolla, Segnet: a deep convolutional encoder-decoder architecture for image segmentation, *IEEE Trans. Pattern Anal. Mach. Intell.* 39 (12) (2017) 2481–2495.
- [61] P. Isola, J.-Y. Zhu, T. Zhou, A.A. Efros, Image-to-image translation with conditional adversarial networks, in: Proceedings of the IEEE conference on computer vision and pattern recognition, 2017, pp. 1125–1134.
- [62] Y. Zhu, N. Zabaras, Bayesian deep convolutional encoder-decoder networks for surrogate modeling and uncertainty quantification, *J. Comput. Phys.* 366 (2018) 415–447.
- [63] G. Huang, Z. Liu, L. Van Der Maaten, K.Q. Weinberger, Densely connected convolutional networks, in: Proceedings of the IEEE conference on computer vision and pattern recognition, 2017, pp. 4700–4708.
- [64] K. He, X. Zhang, S. Ren, J. Sun, Deep residual learning for image recognition, in: Proceedings of the IEEE conference on computer vision and pattern recognition, 2016, pp. 770–778.
- [65] R.K. Srivastava, K. Greff, J. Schmidhuber, Training very deep networks, *Adv. Neural Inf. Process. Syst.* 28 (2015).
- [66] S. Ioffe, C. Szegedy, Batch normalization: accelerating deep network training by reducing internal covariate shift, in: International conference on machine learning, PMLR, 2015, pp. 448–456.
- [67] X. Glorot, A. Bordes, Y. Bengio, Deep sparse rectifier neural networks, in: Proceedings of the fourteenth international conference on artificial intelligence and statistics, JMLR Workshop and Conference Proceedings, 2011, pp. 315–323.
- [68] N. Kanopoulos, N. Vasanthavada, R.L. Baker, Design of an image edge detection filter using the Sobel operator, *IEEE J. Solid-State Circuit.* 23 (2) (1988) 358–367.
- [69] M. Wang, N. Pan, J. Wang, S. Chen, Mesoscopic simulations of phase distribution effects on the effective thermal conductivity of microgranular porous media, *J. Colloid Interface Sci.* 311 (2) (2007) 562–570.
- [70] Z. Shan, A.M. Gokhale, Representative volume element for non-uniform microstructure, *Comput. Mater. Sci.* 24 (3) (2002) 361–379.
- [71] T. Kanit, S. Forest, I. Galliet, V. Mounoury, D. Jeulin, Determination of the size of the representative volume element for random composites: statistical and numerical approach, *Int. J. Solids Struct.* 40 (13) (2003) 3647–3679.
- [72] Z. Mao, A.D. Jagtap, G.E. Karniadakis, Physics-informed neural networks for high-speed flows, *Comput. Methods Appl. Mech. Eng.* 360 (2020), 112789.
- [73] M. Dondero, A.P. Cisilino, J.M. Carella, J.P. Tomba, Effective thermal conductivity of functionally graded random micro-heterogeneous materials using representative volume element and BEM, *Int. J. Heat Mass Transf.* 54 (17) (2011) 3874–3881.
- [74] M. Turkyilmazoglu, Effective computation of solutions for nonlinear heat transfer problems in Fins, *J. Heat Transf.* 136 (9) (2014), 091901.
- [75] S. Mosayebidorcheh, D.D. Ganji, M. Farzinpoor, Approximate solution of the nonlinear heat transfer equation of a fin with the power-law temperature-dependent thermal conductivity and heat transfer coefficient, *Propuls. Power Res.* 3 (1) (2014) 41–47.
- [76] M. Alnæs, J. Blechta, J. Hake, A. Johansson, B. Kehlet, A. Logg, C. Richardson, J. Ring, M.E. Rognes, G.N. Wells, The FEniCS project version 1.5, *Arch. Numer. Softw.* 3 (100) (2015) 9–23.
- [77] S.P. Adhikari, H. Yang, H. Kim, Learning semantic graphics using convolutional encoder-decoder network for autonomous weeding in paddy, *Front. Plant Sci.* 10 (2019) 1404.
- [78] L. Lu, R. Pestourie, W. Yao, Z. Wang, F. Verdugo, S.G. Johnson, Physics-informed neural networks with hard constraints for inverse design, *SIAM J. Sci. Comput.* 43 (6) (2021) B1105–B1132.
- [79] J. Yu, L. Lu, X. Meng, G.E. Karniadakis, Gradient-enhanced physics-informed neural networks for forward and inverse PDE problems, *Comput. Methods Appl. Mech. Eng.* 393 (2022), 114823.
- [80] Z. Chai, H. Liang, R. Du, B. Shi, A lattice boltzmann model for two-phase flow in porous media, *SIAM J. Sci. Comput.* 41 (4) (2019) B746–B772.
- [81] A. Krishnapriyan, A. Gholami, S. Zhe, R. Kirby, M.W. Mahoney, Characterizing possible failure modes in physics-informed neural networks, *Adv. Neural Inf. Process. Syst.* 34 (2021) 26548–26560.
- [82] A. Paszke, S. Gross, F. Massa, A. Lerer, J. Bradbury, G. Chanan, T. Killeen, Z. Lin, N. Gimelshein, L. Antiga, PyTorch: an imperative style, high-performance deep learning library, *Adv. Neural Inf. Process. Syst.* 32 (2019).